

A cell lens model for transverse modes in optofluidic intracavity spectroscopy

Weina Wang and Kevin L. Lear, *IEEE Member*

Abstract— **Optofluidic intracavity spectroscopy of individual cells from canine hemangiosarcoma and canine lymphoma cancer cell lines exhibit relatively uniformly spaced multiple transverse modes repeated in each free spectral range of a microfluidic Fabry-Pérot cavity while similar spectra of healthy canine monocytes and lymphocytes have minimal or no transverse mode peaks. Modeling of the cells as thin lenses allows paraxial Gaussian beam resonator analysis that produces spectral features that quantitatively match the frequencies of transverse modes and qualitatively agree with the trends in maximum transmission of the modes when aperture losses are included. Cell focal lengths of 600 μm and 300 μm are extracted respectively for canine hemangiosarcoma and lymphoma cells from the ratio of transverse to longitudinal frequency spacing while the spectra of canine monocytes indicate they have a focal length $\geq 580\mu\text{m}$. Under an assumption of constant refractive index, the focal lengths imply a radius of curvature for the top surface of the cells that is much greater than their lateral radius.**

Index Terms— **optofluidic intracavity spectroscopy, transverse mode, cell lens model.**

I. INTRODUCTION

OPTICAL diagnostic tools have been widely used to obtain morphological and refractive index (RI) information from individual biological cells. Non-destructive and non-chemical optical processes such as light scattering, absorption, interference, and diffraction can be used to reveal cells' RI values and spatial dependence, which are related to their size, shape and density of the intracellular structures. Cellular morphology and optical properties can indicate the biological state of cells [1], such as cancer [2]. For example, an enlarged nucleus of biological cells has been used as an indication for pre-cancer in clinical diagnosis [3]. Specific techniques for optically interrogating cell structure include forward and side scatter in flow cytometry [4], as well as the use of cell refractometers [5] and Fabry-Pérot (F-P) interferometers [6]. Recently, the authors have been investigating optofluidic intracavity spectroscopy (OFIS) [7]-[9] as a passive cavity form of single cell interferometry derived from the biocavity laser [10]. Optofluidics is a term used to describe the

intersection of photonics and microfluidics [11], and it has been used to investigate physical and properties of single living cell [12]-[13]. OFIS uses a microfluidic structure that is compatible with lab-on-a-chip concepts and does not require a laser source. It provides spectral information that promises to allow simultaneous determination of multiple optical parameters from individual cells.

Recently, OFIS was used to differentiate canine hemangiosarcoma (HSA) and monocytes with great statistical significance [9]. Some notable spectral characteristics were found and motivate a new optical model for optical modes of cells inside a resonant cavity. In particular, previous observations [8]-[9] indicated that OFIS transmission spectra of cancerous cells contained more numerous and stronger transverse modes than spectra of healthy blood cells. Reproduction of these features in the apertured Gaussian beam analysis presented here provides further insight into the relationship between OFIS spectra and cellular shape, size, and refractive index.

This paper is organized into sections on an OFIS overview, the optical model, data analysis and conclusions. Section II reviews the OFIS detection mechanism and experimental methods, as well as summarizes recent results on differentiation of canine HSA and baseline monocytes to provide motivation for better models. A new optical model that treats a cell settled at the channel bottom as an optical lens is presented in Section III, followed by insights on cellular profiles revealed when this optical model is applied to previously reported OFIS data in Section IV.

II. OFIS OVERVIEW

A. OFIS detection mechanism

The OFIS technique utilizes optical refraction, diffraction and interference effects in a microfluidic resonator to produce characteristic transmission spectra of individual cells. As illustrated in Fig. 1(a), a plane-plane F-P cavity filled with fluid of a homogenous RI, n_{fluid} , exhibits longitudinal transmission peaks at resonant frequencies $\nu_q = q\Delta\nu_{\text{long}}$ that are integer multiples of the free spectral range (FSR), $\Delta\nu_{\text{long}} = c/2n_{\text{fluid}}L_{\text{cav}}$, of the cavity where q is the longitudinal mode index, c is the speed of light in vacuum and L_{cav} is the cavity length. As shown in Fig. 1(b)-(d), placing a cell of RI $n_{\text{cell}} > n_{\text{fluid}}$ into the F-P cavity changes its resonant modes, due to the local RI change, both increasing the cavity's optical length through the cell, and inducing lateral optical confinement leading to transverse modes. Hence the number, position, and magnitude of transmission peaks corresponding to multiple

Manuscript received August 1st, 2009.

W. Wang is with the Dept. of Electrical and Computer Engineering, Colorado State University, 80523, USA.

K. L. Lear is with the Dept. of Electrical and Computer Engineering and School of Biomedical Engineering, Colorado State University, 80523, USA (e-mail: Kevin.Lear@colostate.edu, Tel: 970-491-6600).

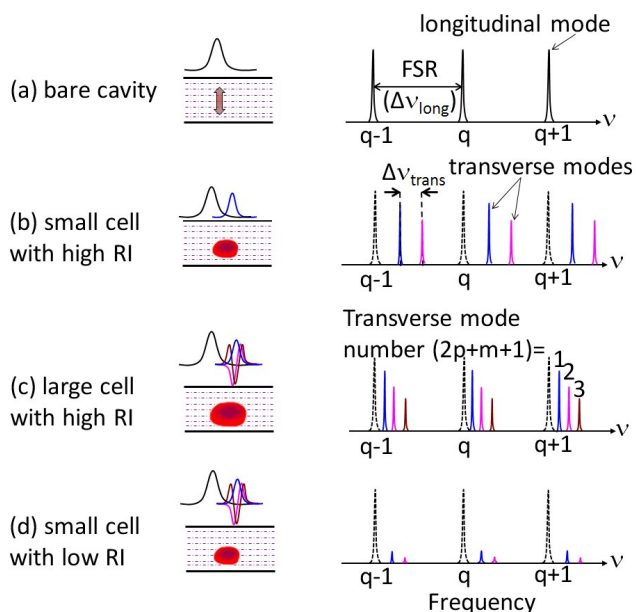


Fig. 1. Schematic diagrams of resonators with different cell sizes and RI and the associated spectra to illustrate the operating principles of OFIS.

transverse modes will be affected by the cell's index profile. Observation of transverse modes in earlier work [8] indicated that cells not only induced a longitudinal mode shift, but also caused important transverse optical confinement effects. Compared to consideration of optical length alone, lateral confinement increases the resonant frequency of the fundamental mode and, by a larger amount, the higher order modes [8]. Larger cells, as shown in Fig. 1(c), or lower RI cells, as shown in Fig. 1(d), provide weaker optical confinement and thus lead to smaller transverse mode spacing, $\Delta\nu_{\text{trans}}$, compared to the spectra of a small, high RI cell, as seen in Fig. 1(b). If optical confinement is weak and the cell is small, larger diffraction losses will decrease the transmission of transverse modes as illustrated in Fig. 1(d). The effects of cell size and refractive index will be discussed quantitatively in Section III. In general, the transverse mode spectrum of a resonator containing a cell is altered as the RI profile and size of cells changes, providing a probe of the cell's optical structure, including cell size, shape, and refractive index attributed to protein content. This information can be used to distinguish different cell types.

B. Experimental methods

A cell is placed in a microresonator on an OFIS chip to acquire its characteristic transmission spectrum. Microfluidic passive F-P cavities were fabricated with the cross-section shown in Fig. 2. In the fabrication sequence, microscale channels were etched into Pyrex glass substrates before a $R=96\%$ reflectivity dielectric mirror (Dominar, Inc.) was coated onto the etched substrates as well as unetched glass superstrates that were then brought together and bonded with epoxy to form a microfluidic resonator. For measurements, cells were delivered by pressure driven flow through a

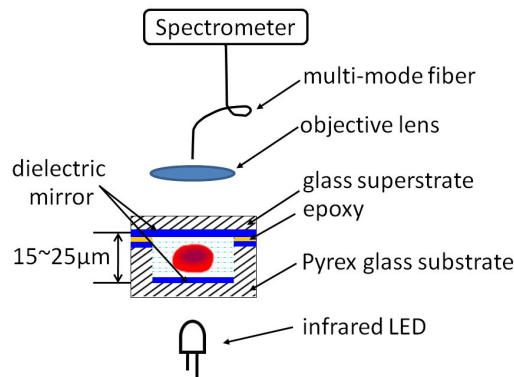


Fig. 2. Cross section view of an OFIS chip and apparatus

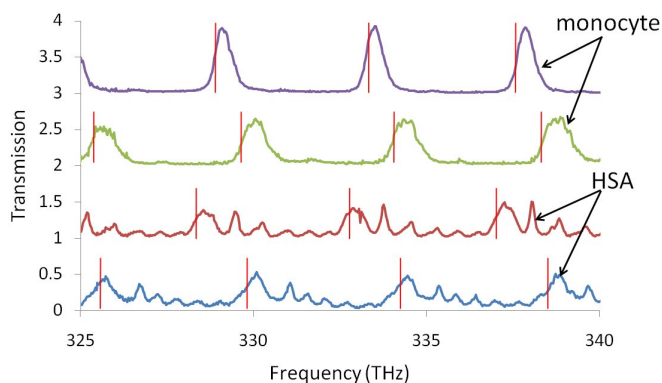


Fig. 3. Normalized transmission spectra of HSA cells and monocytes in a $25\mu\text{m}$ deep cavity. Vertical lines indicate the longitudinal mode resonant frequencies of the fluid filled F-P cavity without cells.

NanoPorts® system (N-124H, Upchurch Scientific) into this resonant cavity. Transmission spectra were collected from individual cells that temporarily settled at the channel bottom while the OFIS chip was bottom illuminated with a high power infrared LED (L2690-02, Hamamatsu). Transmitted light relayed by an objective lens was directed to a fiber coupled spectrometer (HR2000, Ocean Optics). The multimode fiber core acts as a spatial filter with an approximately $10\mu\text{m}$ diameter image in the plane of the channel. The core image was aligned with individual cell positions by translating the entire chip relative to the optical system. Various channel depths were used to collect transmission spectra of cells from cancer cell lines, including canine lymphoma [8] and canine HSA [9], and from baseline non-cancerous blood cells, including canine lymphocytes and monocytes.

C. Recent results on canine HSA and monocytes

The transmission spectra of 24 single cells from canine HSA-DEN cell line and 24 baseline non-cancerous monocytes in $25\mu\text{m}$ and $22\mu\text{m}$ deep cavities were collected and analyzed. HSA is a common canine cancer, and the HSA-DEN cell line used in this study was established in the laboratory of Thamm et al. [14]. Examples of typical normalized transmission

spectra of individual HSA and monocyte cells in a 25 μm deep cavity are given in Fig. 3, which shows approximately three FSRs near the 900nm peak wavelength of the LED. The cell spectra were taken at different locations in the channel where the cells settled. The slowly varying channel thickness, due to a mirror tilt of approximately 0.1 $^\circ$, slightly shifted the 4.4THz FSR of each spectrum. For reference, the longitudinal mode frequencies of the cavity, marked by vertical lines in the figure, were obtained at each cell's location by flowing the cells out of the optical path. These location specific longitudinal frequencies without cells are referred to as "bare cavity" frequencies. Mirror tilt and surface roughness dropped the finesse of the F-P cavity to 13 from the ideal value of 61 expected for $R=96\%$ reflectivity mirrors, but the lower finesse was still sufficient to resolve multiple transverse peaks in cell spectra. Even with the cells present, attenuated and broadened peaks still occur at the bare cavity frequencies, presumably due to some residual light that is not coupled to the cell or light that is scattered from regions outside the cell.

Importantly, the majority of HSA cells induced several new well-defined peaks with significant transmission ($T > 0.1$) that are attributed to transverse modes and are repeated within each FSR. Such transverse mode peaks were absent or significantly weaker in the non-cancerous monocyte spectra. The number and strength of transverse modes from cancer cells was sufficient to raise the mean and standard deviation of transmission between bare cavity frequencies so that these parameters could be used to discriminate cancer cells from healthy cells with 95% sensitivity and 98% specificity as presented in reference [9] which also includes details of the spectral normalization procedure. The moderately uniform spacing of the peaks and decreasing maximum transmission at higher frequencies within each FSR is reminiscent of the classical spectra of nearly planar conventional stable resonators [15] and motivates the resonator analysis presented in Section III.B. Decreasing levels of transmission for higher frequency and thus higher order transverse modes suggest incorporation of diffraction loss in an optical model. Thus the new model presented in this paper employs an apertured paraxial Gaussian beam method and reveals the expected dependency on cell size and focusing strength.

III. OPTICAL MODELS

Two approaches to obtaining approximate solutions for the lateral field profiles and frequencies of transverse modes in a plane-plane microresonator with a localized higher index structure are (A) to treat the configuration as an effective waveguide distributed along the entire length of the resonator and (B) to model it within the paraxial beam approximation while regarding the high index object as an ideal thin lens. The former approach was adopted for an initial analysis of the effects of transverse confinement on longitudinal mode shifts in an OFIS study of canine lymphoma [8] and is briefly reviewed next. Application of the latter approach to OFIS spectra of another canine cancer, HSA, is discussed in detail

for the first time in Section III.B. In both approaches, the higher index structure of the cell provides lateral optical confinement of the beam.

A. Review of effective index model analysis

The microcavity effective index method [16] used in [8] provides a mechanism for modeling a short resonator containing an actual index profile, $n(x,y,z)$, that varies along the z -direction (parallel to the resonator axis) by replacing it with an effective lateral index profile $n_{\text{eff}}(x,y)$ that is independent of longitudinal position in the resonator. The effective index profile is obtained at each lateral position by determining the resonant longitudinal wavevectors, $k_z(x,y)$, of contrived one-dimensional cavities with the same longitudinal index structure at that lateral position but with no lateral index dependence. The normalized variation in the effective index is then taken to equal the normalized variation in the resonant wavevector, i.e. $\Delta n_{\text{eff}}(x,y)/n_{\text{eff}}(0,0) \approx k_z(0,0)\Delta(1/k_z(x,y))$.

A concentric, homogeneous RI, double sphere model of cells, similar to those adopted for optical scattering analysis [17]-[18] was employed in conjunction with the effective index approximation to quantitatively analyze measured canine lymphoma OFIS spectra and extract nuclear size and RI information of the cells [8]. Canine lymphocytes were used as a control for the two lymphoma cell lines investigated, and Fig. 4 shows typical lymphoma and lymphocyte spectra from the 15.8 μm deep cavity used in that study.

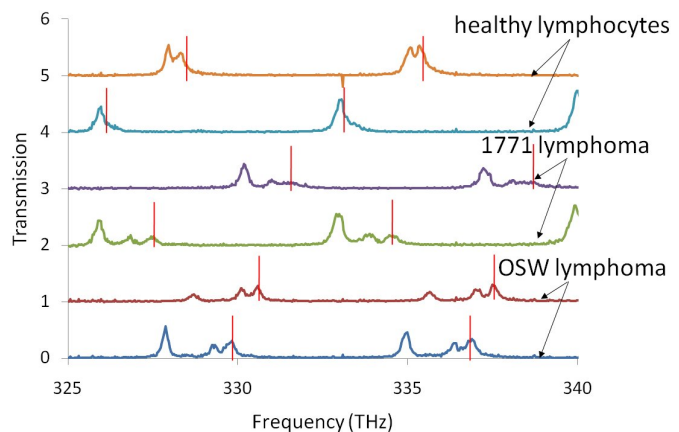


Fig. 4. Normalized transmission spectra of healthy canine lymphocytes and cancerous lymphoma cells from two different cell lines, OSW and 1771, in a 15.8 μm deep cavity, where vertical lines indicate the bare cavity modes adjacent to each cell.

Cells from both lymphoma cell lines exhibited multi-mode behavior with two to three clear transmission peaks in each FSR. The primary peak, attributed to the fundamental mode, was well separated from the bare cavity resonances obtained at the test locations when the cell was removed. The wavelength shift between the bare cavity position and cell's fundamental mode was remarkably repeatable for different cells from the same cell line, with relative standard deviations of 0.5% and 2.0% for the mode shifts of the two types of lymphoma. The lymphocyte control spectra had a fundamental mode as well,

but no higher order transverse modes were observed for these non-cancerous cells. The lymphocytes also caused very repeatable wavelength shifts with a relative standard deviation of 1.4%. Statistical analysis showed that the lymphocyte and lymphoma cells could be properly categorized based on wavelength shift with a probability of error less than 10^{-14} [9].

Despite the successes of the double sphere effective index model in allowing extraction of refractive indices based on fundamental mode shifts while accounting for transverse confinement, it did not provide appropriate predictions of transverse mode number or position. The model predicted far more bound, high order transverse modes than were observed both for lymphoma and lymphocytes. Further, the computed wavelengths of the lower order transverse modes did not readily match the few peak wavelengths observed in multimode spectra. And since the effective index model provides no information on diffraction loss, it also cannot predict the relative magnitude of each mode's transmission peak. The absence of many expected modes in the experimental spectra could be attributed to excessive diffraction loss of the highest order modes, but the equivalent waveguide predicted by the microcavity effective index model allows no diffraction loss for any bound mode, nor is the longitudinal position of the cell within the cavity properly taken into consideration. The lack of agreement in transverse mode peak position and transmission magnitude, as well as consideration of cell deformability calls into question the validity of the microcavity effective index and spherical cell models in this application. In order to evaluate other simple computational methods that could more readily incorporate diffraction loss and additional information from higher order transverse modes, an apertured paraxial Gaussian beam model is described in the following sub-section.

B. Cell lens model

Spectral similarities motivate treatment of the cell loaded plane-plane cavity for OFIS as a classic planar-concave mirror resonator using paraxial Gaussian beam analysis as described in optics textbooks [15]. Specifically, a cell settled on the bottom mirror is assumed to act as a thin lens of focal length f_{cell} and lateral radius a inside a plane-plane cavity, as pictured in Fig. 5. The resulting transverse mode spectrum depends on a , L_{cav} , and f_{cell} . Additionally, the cell is anticipated to cause large diffraction loss for the portion of Laguerre-Gaussian mode profiles that extend beyond the cell radius, and thus the

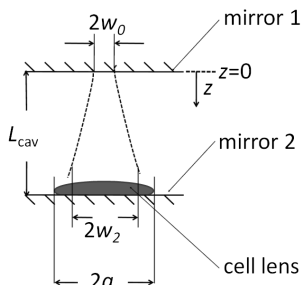


Fig. 5. Cell lens model of cell-loaded F-P cavity

cell is treated as opaque for $r > a$. The goal of the following analysis is to analytically relate the transverse mode frequencies and loss to experimentally observed spectra. The resulting relationships are used in Section IV to extract f_{cell} and to estimate the shape of the cells' top surface from experimental transmission spectra. While the cell surface is likely to have significant aspherical aberrations and the inclusion of apertures in cavities is known to perturb the eigenmodes from ideal Laguerre-Gaussian solutions [19], these issues are neglected in the following analysis for purposes of simplification.

The cell-loaded cavity can be considered as a half-symmetric resonator pictured in Fig. 5 with a Gaussian beam waist of radius w_0 at the plane mirror far from the lens. By analogy to a plane-concave mirror resonator of length L_{cav} , the beam waist at the upper mirror is [15]

$$w_0 = \sqrt{\frac{L_{\text{cav}} \lambda}{\pi} (f_{\text{cell}} / L_{\text{cav}} - 1)^{1/2}} \quad (1)$$

where λ is the wavelength inside the cavity. The beam radius at the cell, or equivalently the adjacent bottom mirror, is

$$w_2 = \sqrt{\frac{f_{\text{cell}} \lambda}{\pi} (f_{\text{cell}} / L_{\text{cav}} - 1)^{-1/2}} \quad (2)$$

The resonance frequencies of the Laguerre-Gaussian modes in the cylindrically symmetric cavity are

$$\nu_{qpm} = q \Delta \nu_{\text{long}} + (2p + m + 1) \Delta \nu_{\text{trans}} \quad (3)$$

where q , p , and m are the integer longitudinal, radial, and azimuthal mode indices, $\Delta \nu_{\text{trans}}$ is the transverse mode spacing, and the g parameter is

$$g = 1 - 2L_{\text{cav}} / f_{\text{cell}} \quad (4)$$

Note that in an ideal resonator, all of the transverse modes are evenly spaced in frequency. An important relationship for the subsequent analysis of cells is the ratio of transverse to longitudinal mode spacing, $\Delta \nu_{\text{trans}} / \Delta \nu_{\text{long}}$, which is related to the strength of focusing in the cavity and the Gouy phase shift of transverse modes. For the most strongly focused stable configuration, a concentric resonator where $f_{\text{cell}} = L_{\text{cav}}$, the ratio is $\Delta \nu_{\text{trans}} / \Delta \nu_{\text{long}} = 1$, and the ratio is $\Delta \nu_{\text{trans}} / \Delta \nu_{\text{long}} = 1/2$ for a confocal resonator with $f_{\text{cell}} = 2L_{\text{cav}}$. Solving the relationship between the g parameter with the transverse mode spacing and equation (4) gives the cell's focal length as

$$f_{\text{cell}} = \frac{L_{\text{cav}}}{\sin^2\left(\frac{\pi}{2} \cdot \Delta \nu_{\text{trans}} / \Delta \nu_{\text{long}}\right)} \quad (5)$$

This expression can be rigorously derived from standard resonator theory for Gaussian transverse mode frequencies [15]. The f_{cell} value of each cell can be readily calculated from the measured transverse to longitudinal mode spacing ratio and known cavity length obtained from the bare cavity FSR using equation (5). Once the f_{cell} value is found for each cell, it can then be used to extract the radius of curvature for the cell surface. The bottom of the cell is assumed to be flat against the bottom mirror of the channel while the top side is convex. The lens maker's equation for a thin plano-convex lens of constant

RI n_{cell} then gives the radius of curvature as

$$R_c = f_{\text{cell}} \cdot (n_{\text{cell}} - n_{\text{fluid}}) \quad (6)$$

Note that it is likely that this is only the curvature for the top surface of the cell, with a smaller radius of curvature at the sides of the cell as pictured in Fig. 5, so that R_c cannot be used to calculate cell thickness.

Beyond the relationship between focal length and transverse mode frequencies, the intensity distribution of various transverse modes is considered to estimate optical losses that impact the maximum transmission of each transverse mode. The incident LED light excites many Laguerre-Gaussian transverse modes but only the lower order ones have sufficiently narrow beam profiles to avoid large diffraction losses when interacting with the fixed radius cell. The field profile of the Laguerre-Gaussian modes [15] is

$$E_{pm}(r, w(z)) = \sqrt{\frac{2p!}{(1+\delta_{0m})\pi(m+p)!}} \cdot \frac{(\sqrt{2}r)^m}{w(z)} \cdot L_p^m \cdot e^{-\frac{r^2}{w(z)^2}} \quad (7)$$

where r is the radial position, z is the longitudinal position, $w(z)$ is the beam radius, $\delta_{0m} = 1$ if $m = 0$ and is zero for $m > 0$, and the generalized Laguerre polynomials L_p^m are [20]:

$$\begin{aligned} L_0^{(m)}(x) &= 1 \\ L_1^{(m)}(x) &= -x + m + 1 \\ L_2^{(m)}(x) &= \frac{x^2}{2} - (m+2)x + \frac{(m+2)(m+1)}{2} \\ L_3^{(m)}(x) &= \frac{-x^3}{6} + \frac{(m+3)x^2}{2} - \frac{(m+2)(m+3)x}{2} + \frac{(m+1)(m+2)(m+3)}{6} \\ &\vdots \end{aligned} \quad (8)$$

While the beam radius parameter, $w(z)$, does not depend on the mode indices p and m , higher order modes have broader intensity profiles as shown in Fig. 6. The example mode profiles in the figure are computed at a distance of $20\mu\text{m}$ from a beam waist of $w_0 = 4\mu\text{m}$ – dimensions consistent with a $20\mu\text{m}$ cavity length and $600\mu\text{m}$ focal length. If the cell causing the focusing had a radius of $a = 10\mu\text{m}$, then almost all of the

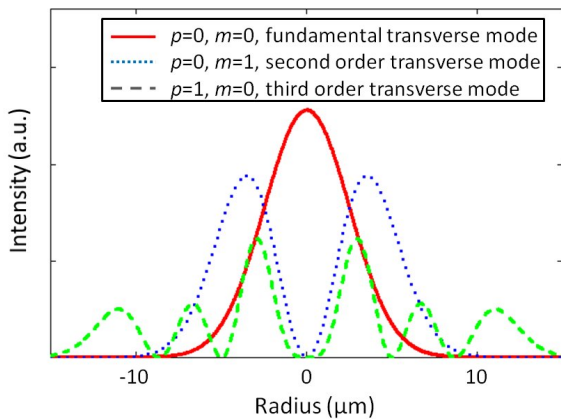


Fig. 6. Intensity profile of the fundamental and two higher order Laguerre-Gaussian modes after they propagate $20\mu\text{m}$ away from a beam waist of $w_0 = 4\mu\text{m}$.

fundamental mode would fall within the cell radius, but the third lobe of the ($p = 1, m = 0$) mode would almost completely miss the cell. The portion that misses the cell lens becomes diffraction or clipping loss, causing the maximum transmission of that mode to decrease.

For the analysis presented here, it is assumed that the mode tails at a radial position greater than the cell radius will be lost, resulting in mode dependent diffraction loss. The loss for each mode is taken to be the integral of the normalized intensity beyond the cell of radius, $r > a$, since light in that region will not be refocused by the lens but will continue to diffract. Thus the fraction of the optical power that is not lost on each roundtrip through the cell can be thought of as the mode specific transmission of an aperture of radius a ,

$$T_a = \frac{2\pi \int_0^a E_{pm}^2(r, w_2) r \cdot dr}{2\pi \int_0^\infty E_{pm}^2(r, w_2) r \cdot dr} = \frac{\int_0^{r/a=1} E_{pm}^2\left(\frac{r}{a}, \frac{w_2}{a}\right) \frac{r}{a} d\left(\frac{r}{a}\right)}{\int_0^{r/a=\infty} E_{pm}^2\left(\frac{r}{a}, \frac{w_2}{a}\right) \frac{r}{a} d\left(\frac{r}{a}\right)} \quad (9)$$

Note that this is the roundtrip loss based on the approximation that the lens is effectively in the plane of the bottom mirror and that negligible diffraction occurs during the beam propagation from the cell to the lower mirror and back to the cell.

The calculated aperture or cell transmission, T_a , can be related to the expected OFIS transmission spectrum by noting that diffraction loss out of the mode inside the cavity effectively mismatches the mirrors of nominally identical reflectivity, R , causing a reduction in the maximum transmission for each mode in the F-P cavity to a value less than unity. The maximum transmission of a F-P cavity with internal loss [15] that results from an aperture with transmission of T_a is

$$T_{\text{max}} = \frac{(1-R)^2 T_a}{(1-R\sqrt{T_a})^2} \quad (10)$$

Fig. 7 illustrates the maximum transmission of different modes calculated with equations (7)-(10) with the parameters $L_{\text{cav}} = 25\mu\text{m}$, $f_{\text{cell}} = 632\mu\text{m}$, and $a = 7.8\mu\text{m}$. These are values for HSA cell experiments as discussed in Section IV. According to equation (3), the transverse frequency contribution depends on $2p+m+1$, creating some degeneracy in mode frequency.

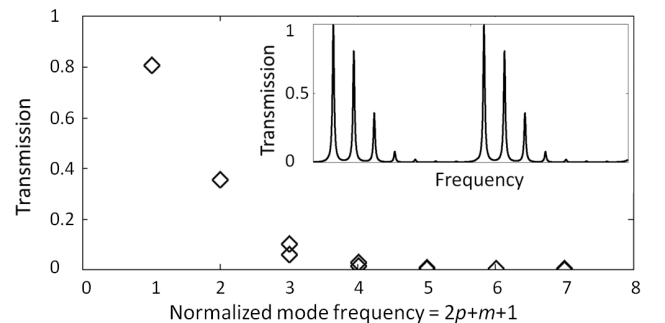


Fig. 7. Maximum transmission for different transverse modes calculated from parameters described in the text. Inset shows simulated transmission spectrum of an ideal cell-loaded F-P cavity.

Thus more than one combination of p and m exist for higher order transverse mode frequencies although modes at the same frequency have comparable maximum transmission. Based on the maximum transmission calculation presented above, a simulated transmission spectrum of an ideal cell-loaded F-P cavity is shown in the inset of Fig. 7. The same L_{cav} , f_{cell} and a parameters from the HSA experiments and $R=96\%$ was used for the simulation.

Fig. 7 clearly shows that the peak transmission decreases as mode order increases, due to the increasing aperture loss. This same trend is observed in the transmission spectrum of HSA cells shown in Fig. 3. Within a transverse mode group, the fundamental mode has the lowest loss and thus the highest transmission of all the transverse modes induced by introducing a HSA cell into the cavity. Within each FSR, transverse modes at higher frequencies, i.e. higher order modes, have decreasing peak transmission in agreement with the model. Careful quantitative comparison of the model and experimental results shows that the experimental lower order modes have smaller transmission than predicted while the rate of decrease in the experimental peak transmission is not as rapid as the model indicates. These quantitative differences may be due to approximations made to simplify the model, or scattering from cell RI inhomogeneities. Further characterization of the cell-loaded cavity with a thick lens model and inclusion of aberrations and self-consistent solutions of the resonator modes may reduce this disagreement.

The results revealed by the cell lens model not only can be used to analyze transmission spectra that show well-defined, multiple transverse modes, but also is a useful tool to investigate lower bounds on the focal lengths of cells whose transmission spectra don't have observable multiple transverse modes. Consideration of equations (9)-(10) shows that the maximum transverse mode transmission is dependent on the relative mode size, w_2/a . The transmission of the fundamental mode as a function of the w_2/a ratio is shown in Fig. 8. And since the calculated f_{cell} is much longer than the typical cavity lengths, L_{cav} , employed for OFIS, equation (2) can be approximated to show that for the cells in the same cavity, w_2/a is linearly proportional to $f_{cell}^{1/4}/a$, an expression of two parameters that are closely related to the optical and physical properties of cells. Cells that are small in size and have large

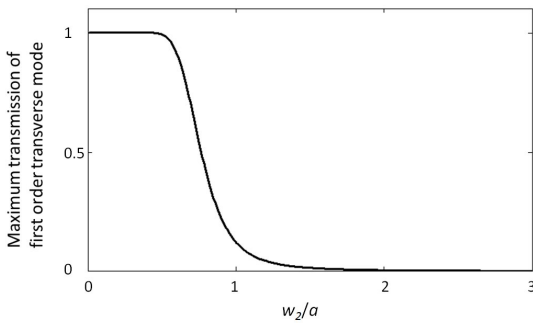


Fig. 8. Transmission of the fundamental mode of cells as a function of the beam to cell radius ratio.

focal lengths have sufficiently large relative mode sizes at the cell that multiple transverse modes are suppressed and thus not observed in their transmission spectra. Using this approach, an observed limit on fundamental mode transmission can be used to estimate a minimum value of focal length, and this rough estimation of f_{cell} can be given by modifying equation (2) into:

$$w_2 / a = \frac{\sqrt[4]{f_{cell}}}{a} \sqrt{\frac{\lambda}{\pi}} \sqrt{L_{cav}} \quad (11)$$

IV. DATA ANALYSIS

In conjunction with the cell lens model discussed above, the ratio of transverse to longitudinal mode spacing of experimental cell transmission spectra are summarized along with cell radii from microscopic observations. The measured data are used to extract focal length information for two cancerous cell types, canine HSA and canine lymphoma, and the focal length of non-cancerous baseline monocytes is estimated based on the maximum transmission of the fundamental mode.

A. Canine HSA

The transverse mode spacing of all HSA cell experiments is summarized in Table I. Transmission spectra were acquired from 24 HSA cells measured in two cavities of different channel depths to verify that the inferred focal length was not dependent on cavity length. The majority of the HSA cells demonstrated multiple transverse mode peaks with moderately uniform frequency spacing although the peaks of 3 cells in the 25 μ m deep channel could not be resolved.

Due to a lack of published refractive index data for canine cancers, $n_{cell}=1.39$ [8], [13] is assumed to be the same for all

	HSA cell number	Number of resolvable peaks	$\Delta \nu_{trans}^{11}$ ($\times 10^{-11}$ Hz)	$\Delta \nu_{trans}/\Delta \nu_{long}$
HSA data collected from 25 μ m deep channel	HSA1	0	-	
	HSA2	6	6.4 \pm 1.0	0.15
	HSA3	6	6.7 \pm 0.7	0.15
	HSA4	6	6.4 \pm 1.7	0.15
	HSA5	0	-	-
	HSA6	6	7.1 \pm 0.5	0.16
	HSA7	6	5.2 \pm 1.1	0.12
	HSA8	0	-	-
	HSA9	6	5.8 \pm 1.0	0.13
	HSA10	6	6.0 \pm 1.0	0.14
	HSA11	6	5.5 \pm 1.7	0.12
	HSA12	6	5.5 \pm 1.2	0.13
	HSA13	4	4.8 \pm 3.6	0.11
	HSA14	3	5.3 \pm 0.3	0.12
	HSA15	3	5.8 \pm 1.8	0.13
	HSA16	3	5.8 \pm 1.2	0.13
HSA data collected from 22 μ m deep channel	HSA1	6	5.9 \pm 0.4	0.11
	HSA2	6	7.4 \pm 0.6	0.14
	HSA3	6	6.8 \pm 1.8	0.13
	HSA4	5	7.0 \pm 1.5	0.14
	HSA5	7	6.1 \pm 1.1	0.12
	HSA6	6	6.2 \pm 1.5	0.12
	HSA7	7	5.2 \pm 1.2	0.10
	HSA8	7	6.3 \pm 0.9	0.12

Table I. Transverse mode spacing summary of HSA in two channels of different cavity depths.

cancerous cells, and $n_{\text{fluid}}=1.333$ for the phosphate buffered saline solution in which cells were suspended. From the spectra of HSA cells in the $25\mu\text{m}$ deep cavity, the cell focal length is calculated to be $f_{\text{cell}} = 632\pm 147\mu\text{m}$, corresponding to a radius of curvature on the cell surface of $36\pm 8\mu\text{m}$, and its lateral radius is estimated to be $a = 7.8\mu\text{m}$. The focal length of HSA cells in the $22\mu\text{m}$ deep cavity is calculated to be $601\pm 137\mu\text{m}$, corresponding to a radius of curvature on the cell surface of $34\pm 8\mu\text{m}$. Although the transmission spectra of HSA cells were acquired from two channels of different cavity depths, there is no statistical difference between the cell focal lengths or the radii of curvature of the top surface of the cells. The radius of curvature of the HSA cell surface is approximately 4 times larger than cell's radius, implying the top plane of the cell is very flat when it is settled at the channel bottom.

B. Canine lymphoma

The transmission spectra of 6 single cells from another canine cancer cell line, lymphoma-1771, were collected in a $21\mu\text{m}$ deep cavity and analyzed. Examples of normalized typical transmission spectra of lymphoma cells are plotted in Fig. 9. Although not as strong as those of the HSA spectra, multiple transverse modes with moderately uniform spacing were identified, and they were repeated in each 5.3THz FSR.

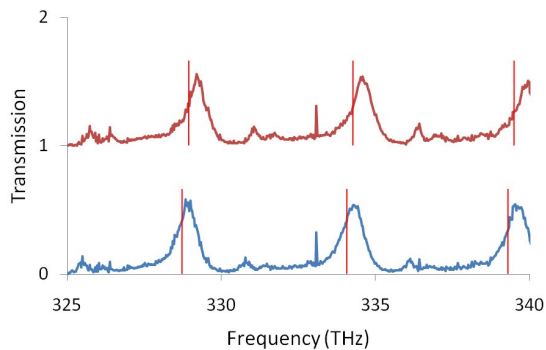


Fig. 9. Normalized lymphoma transmission spectra in a $21\mu\text{m}$ deep channel. (The sharp peak at 333THz was due to the background fluorescent lighting).

The frequency spacing results of all lymphoma-1771 cell experiments are summarized in Table II. The focal length of lymphoma cells is calculated to be $324\pm 44\mu\text{m}$, resulting in a radius of curvature of $18\pm 2.5\mu\text{m}$. Based on microscopic measurements [8], their radius was $a = 6.5\mu\text{m}$. Note that similar to the HSA cells, the radius of curvature of the lymphoma cell surface is approximately 3 times the cells' lateral radius.

C. Canine monocyte

In general, monocytes have less focusing power than cancer cells due to their smaller index of $n_{\text{cell}} = 1.37$ [21]; and since monocytes are smaller in size, a greater portion of the Laguerre-Gaussian beam falls outside the cell cross-section, causing larger diffraction loss and thus lower transmission peaks. As a result, only the fundamental transverse mode peak with very low transmission is resolvable in the OFIS spectra of monocytes, such as the ones shown in Fig. 3. Since the mode

	lymphoma cell number	Number of resolvable peaks	$\Delta \nu_{\text{trans}}^{11}$ ($\times 10^3$ Hz)	$\Delta \nu_{\text{trans}}/\Delta \nu_{\text{long}}$
lymphoma data collected from $21\mu\text{m}$ deep channel	lymphoma1	4	8.8 ± 0.8	0.17
	lymphoma2	4	9.9 ± 2.0	0.19
	lymphoma3	2	$8.0\pm \text{N/A}$	0.15
	lymphoma4	5	8.8 ± 3.7	0.17
	lymphoma5	4	8.6 ± 1.9	0.16
	lymphoma6	5	8.7 ± 2.7	0.16

Table II. Transverse mode spacing summary of lymphoma-1771

spacing information is not available in this case, equation (5) cannot be applied to determine the cell focal length. However, a lower limit on focal length can be found from equation (11).

For the monocytes in the $25\mu\text{m}$ deep channel, the maximum transmission of the fundamental transverse mode is found to be $T_{\text{max}} \leq 0.08$, corresponding to a ratio of $w_2/a \geq 1.07$, according to Fig. 8. And the monocytes' lateral radius estimated from microscopic images was $a = 5.5\mu\text{m}$. According to equation (11), $f_{\text{cell}} \geq 579\mu\text{m}$, making the monocyte focal length at least comparable to that of HSA and larger than the focal length of the lymphoma cells. The lower bound on the radius of curvature of the top surface of monocytes is $21\mu\text{m}$, roughly 4 times the lateral radius.

D. Comparison of neoplastic and non-neoplastic cells

The focal length, radius of curvature, as well as the ratio of cell's surface radius of curvature to its lateral radius is summarized in Table III for the three types of cells investigated. The size of canine monocytes is comparable to that of lymphoma cells, but monocytes appear to have a much longer focal length (i.e., less focusing power), presumably because non-cancerous cells are less protein rich than cancerous cells. This result is consistent with the general understanding that rapid cell division and growth [1] in cancerous cells correlates with more high RI protein ($n = 1.50$ [22]) in the nucleus.

cell type	L_{cav} (μm)	a (μm)	f_{cell} (μm)	R_c (μm)	R_c/a
canine HSA	25	7.8	632 ± 147	36 ± 8.4	4.6
canine HSA	22	7.8	601 ± 137	34 ± 7.8	4.4
canine lymphoma	21	6.5	324 ± 44	18 ± 2.5	2.8
canine monocyte	25	5.5	≥ 579	≥ 21	≥ 3.8

Table III. Compare between neoplastic and non-neoplastic cells.

V. CONCLUSION

In summary, individual cells have been modeled as simple lenses in a paraxial Gaussian beam analysis to explain multiple transverse mode transmission spectra obtained in OFIS. Cancerous cells from canine HSA and lymphoma cell lines exhibit multiple, notable transverse modes with relatively uniform frequency spacing and decreasing peak transmission for higher order modes while multiple transverse modes are

not readily observed for non-cancerous canine lymphocytes and monocytes. The absence of transverse modes in the OFIS spectra of the latter cells is attributed to the greater diffraction loss associated with these smaller cells with long focal lengths. The decreasing peak transmission of higher order modes in cancer cells is also attributed to increased diffraction loss.

The model and associated analysis allows extraction of cell focal lengths based on the ratio of transverse to longitudinal mode spacing that are apparent in OFIS spectra. The small value of maximum transmission for monocyte modes was used to establish a lower bound on the focal length of these cells. Focal lengths for lymphoma are smaller than for HSA, and focal lengths for monocytes are larger than for lymphoma and possibly HSA. In all cases, the radius of curvature of the cell surface, when the cell is settled at the bottom of the channel, is multiple times the observed lateral radius of the cells, indicating significant flattening of the cell surface. The Gaussian beam model results in theoretical spectra that are more consistent with experimental OFIS spectra than spectra predicted by the effective index approximation.

Thus the Gaussian beam model was found to be useful in explaining the frequency spacing and trends in transmission peak amplitudes for OFIS. However, the Gaussian beam model overestimates the maximum transmission of the fundamental mode and predicts a faster decline in peak transmission with increasing mode number than is actually observed. Future improvements to the analysis should include a thick rather than thin lens model, scattering from cell RI inhomogeneities, inclusion of aberrations, and self-consistent solutions of the resonator modes. Shorter cavities are expected to reduce diffraction losses and increase the transmission of higher order modes for all cells.

ACKNOWLEDGMENT

The authors thank D. Thamm and B. Rose at the CSU Department of Clinical Sciences for providing cells and technical assistance, L. Netherton and H. Cutler for operating experiments, and D. Kisker for useful discussions.

REFERENCES

- [1] V. Backman, et al., "Detection of preinvasive cancer cells," *Nature*, vol. 406, pp. 35-36, Jul 2000.
- [2] K. Sokolov, M. Follen and R. Richards-Kortum, "Optical spectroscopy for detection of neoplasia," *Current Opinion in Chemical Biology*, vol. 6, pp. 651-658, Oct 2002.
- [3] J. Beuthan, O. Minet, J. Helfmann, M. Herrig and G. Muller, "The spatial variation of the refractive index in biological cells," *Physics in Medicine and Biology*, vol. 41, pp. 369-382, Mar 1996.
- [4] H. M. Shapiro, *Practical Flow Cytometry*, 4th Edition, Wiley, Hoboken, NJ, 2003.
- [5] J. Y. Lee, C. W. Lee, E. H. Lin and P. K. Wei, "Single live cell refractometer using nanoparticle coated fiber tip," *Applied Physics Letters*, vol. 93, Oct 2008.
- [6] L. K. Chin, et al., "Differential single living cell refractometry using grating resonant cavity with optical trap," *Applied Physics Letters*, vol. 91, no. 243901, Dec 2007.
- [7] H. Shao, D. Kumar, and K. L. Lear, "Single-cell detection using optofluidic intracavity spectroscopy", *IEEE Sensors Journal*, vol. 6, pp. 1543-1550, Dec 2006.

- [8] H. Shao, W. Wang, S. E. Lana, and K. L. Lear, "Optofluidic intracavity spectroscopy of canine lymphoma and lymphocytes," *IEEE Photonics Technology Letters*, vol. 20, no. 5-8, pp. 493-495, Mar-Apr, 2008.
- [9] W. Wang, D. W. Kisker, D. H. Thamm, H. Shao, and K. L. Lear, "Optofluidic Intracavity Spectroscopy of Canine Hemangiosarcoma," *IEEE Transactions on Biomedical Engineering*, submitted for publication.
- [10] P. L. Gourley, "Biocavity laser for high-speed cell and tumour biology," *Journal of Physics D-Applied Physics*, vol. 36, no. 14, pp. R228-R239, Jul 2003.
- [11] S. H. Ahn and Y. K. Kim, "Proposal of human eye's crystalline lens-like variable focusing lens," *Sensors and Actuators A-Physical*, vol. 78, pp. 48-53, Nov 1999.
- [12] W. Z. Song, et al., "Determination of single living cell's dry/water mass using optofluidic chip," *Applied Physics Letters*, vol. 91 no. 223902, Nov 2007.
- [13] X. J. Liang, A. Q. Liu, C. S. Lim, T. C. Ayi and P. H. Yap, "Determining refractive index of single living cell using an integrated microchip," *Sensors and Actuators A-Physical*, vol. 133, no.2, pp. 349-354, Feb 2007.
- [14] D. H. Thamm, "Miscellaneous Tumors: Hemangiosarcoma", in *Withrow and MacEwan's Small Animal Clinical Oncology*, 4th Edition, S. J. Withrow and D. M. Vail, Ed. Philadelphia: W.B. Saunders, pp. 785-795, 2007.
- [15] A. E. Siegman, *Lasers*, Mill Valley, CA: University Science, Chapter 19, 1986.
- [16] G. R. Hadley, "Effective-index model for vertical-cavity surface emitting lasers", *Optics Letters*, vol. 20, no. 13, pp. 1483-1485, Jul 1995.
- [17] P. M. A. Slood, A. G. Hoekstra and C. G. Figdor, "Osmotic response of lymphocytes measured by means of forward light scattering: theoretical considerations," *Cytometry*, vol. 9, no. 6, pp. 636-641, Nov 1988.
- [18] C. G. Liu and C. E. Capjack, "Effects of cellular fine structure on scattered light pattern," *IEEE Transactions on Nanobioscience*, vol. 5, no. 2, pp. 76-82, Jun 2006.
- [19] T. Li, "Mode selection in an aperture-limited concentric maser interferometer," *Bell System Technical Journal*, vol. 42, no. 6, pp. 2609-2620, 1963.
- [20] G. E. Andrews, R. Askey and R. Roy, "Laguerre Polynomials," *Special Functions*, Cambridge, England: Cambridge University Press, pp. 282-293, 1999.
- [21] V. A. Loiko, G. I. Ruban, O. A. Gritsai, V. V. Berdnik, and N. V. Goncharova, "Mononuclear cells morphology for cells discrimination by the angular structure of scattered light," *10th International Conference on Electromagnetic and Light Scattering by Nonspherical Particles*, Bodrum, Turkey, 17-22 June, 2007.
- [22] M. Kohl, M. Cope, M. Essenpreis and D. Bocker, "Influence of glucose concentration on light scattering in tissue-simulating phantoms," *Optics Letters*, vol. 19, pp. 2170-2172, Dec 1994.

Weina Wang received the B.S. degree in Opto-Electronics from Tsinghua University, Beijing, China in 2004 and M.S. degree in Micro-Electronics from University of Southampton, Southampton, UK in 2006. She is working toward the Ph.D. degree in Electrical and Computer Engineering at Colorado State University, Fort Collins, US, since August 2006. Her research interests include the design and fabrication of optical biosensors and optical modeling of single cell sensing structures.

Dr. Kevin L. Lear (SM'88-M'90) received the B.S.E.E. degree from the University of Colorado, Boulder, in 1984 and the M.S.E.E. and Ph.D.E.E. degrees from Stanford University, Stanford, CA, in 1985 and 1990.

He was a Senior Member of Technical Staff at Sandia National Laboratories, Albuquerque, NM, from 1990 to 1997. In 1997, he became the Chief Scientific Officer at Micro Optical Devices, Inc., Albuquerque: a small business commercializing VCSELs, which was subsequently acquired by Emcore Corporation. In 1999, he joined Colorado State University, Fort Collins, as the Rockwell Anderson Associate Professor of Electrical and Computer Engineering. His research is currently focused on photonic biosensors and components for high-speed optical communication.

Dr. Lear received an IEEE Lasers and Electro-Optics Society Distinguished Lecturer Award in 1996 for his work on VCSELs.